ACS APPLIED MATERIALS & INTERFACES

Research Article

www.acsami.org

Rapid Microwave-Assisted Green Synthesis of 3D Hierarchical Flower-Shaped $NiCo_2O_4$ Microsphere for High-Performance Supercapacitor

Ying Lei,[†] Jing Li,[‡] Yanyan Wang,[†] Li Gu,[‡] Yuefan Chang,[†] Hongyan Yuan,[†] and Dan Xiao*[,†,‡]

[†]College of Chemical Engineering and [‡]College of Chemistry, Sichuan University, 29 Wangjiang Road, Chengdu, Sichuan 610064, PR China

Supporting Information

ABSTRACT: Binary metal oxides with three-dimensional (3D) superstructure have been regarded as desirable electrode materials for the supercapacitor due to the combination of the improved electrical conductivity and effective porous structure. 3D hierarchical flower-shaped nickel cobaltite ($NiCo_2O_4$) microspheres have been fabricated by a rapid and template-free microwave-assisted heating (MAH) reflux approach followed by pyrolysis of the as-prepared precursors. The flower-shaped $NiCo_2O_4$ microspheres, composed of ultrathin nanopetals with thickness of about 15 nm, are endowed with large specific surface area (148.5 m^2 g^{-1}) and a narrow pore size distribution (5−10 nm). The as-fabricated porous flower-shaped $NiCo_2O_4$ microspheres as electrode materials for supercapacitor exhibited high specific capacitance of 1006 F g^{-1} at 1 A g^{-1}, enhanced rate capability, and excellent electrochemical stability with 93.2% retention after 1000 continuous charge−discharge (CD) cycles even at a high current density of 8 A g^{-1}. The desirable integrated performance enables it to be a promising electrode material for the electrochemical supercapacitor (EC).

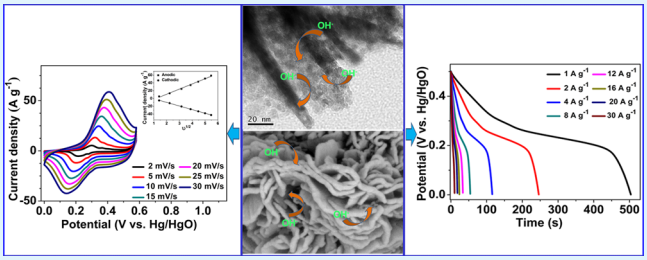

KEYWORDS: *flower-shaped microspheres, microwave-assisted, binary metal oxides, supercapacitor*

1. INTRODUCTION

With the fast-growth of the portable electronic devices and hybrid electric vehicles markets, the demand for high-power energy resources sharply increases.[1,2] Electrochemical capacitors (ECs), also called supercapacitors, as a kind of efficient energy storage devices, which fill the gap between batteries and conventional capacitors due to their satisfactory performance of higher power density and better cycling lifespan over batteries and higher energy density than conventional capacitors, have attracted increasing attention in recent years.[3−5] Currently, the practical applications of supercapacitors are mainly restrained by the lack of high-performance electrode materials readily available from a simple/rapid synthesis method. As we know, the low specific capacitance of conventional carbon-based materials, due to their intrinsic charge storage mechanisms based on reversible adsorption of ion at the electrode/electrolyte interface, and the mechanical degradation of conducting polymers hinder their applications as advanced electrode materials. Fortunately, transition metal oxides/hydroxides endowed with multiple oxidation states/structures capable of rich redox reactions can achieve much higher specific capacitance than the carbon-based materials and conducting polymer materials, which makes them the most promising electrode materials for high-performance supercapacitors.

As a typical transition metal oxide (TMO) electrode material, RuO_2 is regarded as a notable one with remarkably high specific capacitance.[6,7] Nevertheless, the high cost and toxic nature of RuO_2 have impeded its commercial applications. Hence, tremendous efforts have been devoted to searching for and developing alternative electrode materials with low cost, abundant resources, environmental friendliness, and enhanced performance, such as NiO,[8,9] $Ni(OH)_2$,[10,11] Co_3O_4,[12,13] $Co(OH)_2$,[14,15] and MnO_2.[16,17] However, compared with RuO_2, these TMOs/transition metal hydroxides have exhibited inferior electrochemical performance, fundamentally due to their nature of too insulating to support fast electron transport between electrolyte and electroactive species. Therefore, it is imperative to enhance the electrical conductivity of TMOs to meet the requirements of practical application, especially in high-power electric actuators such as electric vehicles and hybrid electric vehicles. Generally, some nanostructured materials are endowed with enhanced kinetics and activity, due to their higher specific surface area (SSA), and shorter pathways for electron and ion transport in comparison with their bulk counterparts.[18] Therefore, the development of nanostructured TMOs with different morphologies undoubtedly provides a promising solution to ameliorate the electrochemical performance of TMO electrode materials. Never-

Received: October 28, 2013
Accepted: January 20, 2014
Published: January 20, 2014

   dx.doi.org/10.1021/am404765y | ACS Appl. Mater. Interfaces 2014, 6, 1773−1780

theless, it is still considered to be a substantive challenge to synthesize TMOs with desirable microstructure, crystallinity, and electrical conductivity.

Among various TMO materials, benefiting from richer redox reaction from both nickel and cobalt ions than from single component nickel oxides or cobalt oxides, spinel nickel cobaltite ($NiCo_2O_4$) exhibits wonderful electrochemical performance such as much better electrical conductivity and superior electrochemical activity.[3,19] These prominent advantages drive it to be a more promising and scalable alternative electrode material for application in high-performance supercapacitors. Various $NiCo_2O_4$ materials with diverse morphologies, such as nanoparticles[20] and nanowires[4,21,22] and being urchin-like,[19] exhibit distinct differences in their electrochemical performance. While some hierarchically three-dimensional (3D) structured metal oxides with two or more levels of structure have caught considerable attention over the past decade due to their high SSA and high density of defects arising from nanometer-sized building blocks,[23] these 3D structures have many potential applications in many fields such as catalysis,[24] batteries,[25,26] chemical sensors,[9] and electrochromic devices.[27] Generally, it is critical for supercapacitors to achieve high SSA and proper pore size appropriate for toilless access for the electrolyte by modulating porous structure of electrode materials. It is well recognized that the charge-storage area for pseudocapacitors is only concentrated in the first few nanometers from the surface. As a result, to improve the usage of active materials, the particle size should be decreased as much as possible. For example, Jiang et al.[11] have prepared extremely uniform $Ni(OH)_2$ with hierarchical 3D nanostructures assembled from ultrathin nanoflakes (thickness of ~7 nm). Compared to the stacked $Ni(OH)_2$ nanoplatelets (thickness of ~22 nm) and randomly arranged hexagonal nanosheets (thickness of ~140 nm), the hierarchical 3D ultrathin nanoflakes nanostructures exhibit a higher specific capacitance of 1715 F g^{-1} at a scan rate of 5 mV s^{-1} with higher rate capability and better cycling stability. In addition, uniform hierarchical 3D nanostructures, assembled from nanoflakes, nanotubes, nanorods, or nanowires, also have exhibited excellent capacitive performance due to their high SSA and appropriate hierarchical 3D porous structures. For example, Wang et al.[19] have synthesized 3D urchin-like $NiCo_2O_4$ consisting of numerous small radial nanorods via a simple hydrothermal method free of any templates. The as-prepared 3D $NiCo_2O_4$ urchins exhibited superior specific capacitance of 1650 F g^{-1} at the current density of 1 A g^{-1} and excellent cycling stability with capacitance loss of only 9.2% after 2000 cycles. These results indicate that some 3D superstructures built from a large sum of small porous nanostructure units (~10 nm in diameter) are more efficient for supercapacitors. Thus, it can be anticipated that the spinel $NiCo_2O_4$ fashioned into 3D hierarchical superstructure composed of porous nanobuilding blocks could be a better choice for the next generation high-performance supercapacitors.

The microwave-assisted heating (MAH) method is a simple and useful technique. It could be considered environmentally friendly for its direct interaction of microwave energy with the reaction system instead of the indirect transfer of energy in the conventional heating method. Therefore, it has been widely applied in chemical reactions and synthesis of porous inorganic materials,[28−30] due to its advantages such as rapid and uniform volumetric heating and dramatic shrinkage in synthesis time.[31−34] Many transition metal oxides/hydroxides with various self-assembled architectures such as α-$Ni(OH)_2$, NiO, Co_3O_4, and Fe_3O_4 have been synthesized by the MAH method.[32−35]

Herein, we report a facile and environmentally friendly MAH synthetic strategy for the preparation of hierarchical flower-shaped microsphere precursors via a rapid sequential crystallization process. The flower-shaped microsphere precursors were easily converted to porous spinel $NiCo_2O_4$ with a well-conserved morphology. The $NiCo_2O_4$ microspheres acting as electrode materials for supercapacitors exhibit high specific capacitance, improved rate capability, and remarkable electrochemical stability even at a high current density. The excellent performance could benefit from the superiority of the hierarchically 3D flower-shaped microstructure and the convenient ion transport within and between the nanopetals.

2. EXPERIMENTAL SECTION

2.1. Materials Synthesis. All the analytical grade chemicals are commercially available and were used as received. Triply distilled water was used during all the experimental processes. In a typical experiment, 1.5 mmol of $CoCl_2{\cdot}6H_2O$, 0.75 mmol of $NiCl_2{\cdot}6H_2O$, and 45 mmol of urea were dissolved in 50 mL of aqueous solution. After vigorous stirring for 20 min at room temperature, the resulting transparent solution was then transferred to a 100 mL three-necked flask. The three-necked flask was placed in the chamber of a microwave chemical reactor (MCR-3, Gong yi, China), the top of which was equipped with a water cooled condenser. The solution was subjected to MAH reflux with microwave radiation power of 320 W at a fixed temperature of 100 °C for 15 min. The clear solution gradually became opaque following the MAH reflux process proceeding. After the reaction mixtures cooling to room temperature, the precipitates were collected by centrifugation and washed with triply distilled water and ethanol for several times. The precursors were dried in a vacuum at 60 °C overnight and then calcinated in air at 300 °C for 2 h with a heating ramp of 5 °C min^{-1} to obtain the black $NiCo_2O_4$ powders.

2.2. Characterization. Crystallite structure of the flower-shaped microsphere samples was established on a Tongda TD-3500 X-ray powder diffractometer (Liaoning, China) with Cu Kα radiation (λ = 0.15148 nm) operating at 30.0 kV and 20.0 mA. The X-ray photoelectron spectra (XPS) were obtained from a Kratos XSAM 800 spectrometer (Manchester, U.K.) with a Mg-Ka X-ray (1253.6 eV) excitation source running at 15 kV, a hemispherical electron energy analyzer, and a multichannel detector. The thermal behavior of the precursors was examined by employing thermogravimetric (TG) and differential thermal analysis (DTA) on a Henven HCT-2 thermal analyzer (Beijing, China). The measurements were performed with a ramping rate of 10 °C min^{-1} from room temperature to 520 °C in air. Field emission scanning electron microscopy (FESEM) images were acquired on a Hitachi S4800 scanning electron microscope (Tokyo, Japan) to examine the morphology of the products. Morphologies of the detailed structures were measured with a FEI Tecnai G2 20 high-resolution transmission electron microscope (TEM) (Hillsboro, OR, USA). N_2 adsorption/desorption was determined by Brunauer−Emmett−Teller (BET) measurements using a QuadrasorbTM SI Automated Surface Area and Pore Size Analyzer (Quantachrome, Instruments, Boynton Beach, FL, USA).

2.3. Electrochemical Measurement. For the electrochemical measurements, the as-prepared sample was mixed with acetylene black as the conducting material and poly(vinyldifluoride) binder, in a weight ratio of 80:15:5. A small amount of *N*-methylpyrrolidinone was then added to the mixtures, and then, the slurries were coated on the nickel foam substrates (surface, 1 cm × 1 cm). After being dried at 80 °C for 2 h, the as-formed electrodes loaded with the active material were then pressed at 10 MPa and then further dried at 80 °C overnight before use. Before and after the sample was dried thoroughly, the nickel foam was weighed. The mass loading of active materials in a nickel foam electrode was about 3.0 mg. The obtained $NiCo_2O_4$ modified electrode was then used as a working electrode.

All the electrochemical measurements of the as-obtained samples were carried out on an Autolab PGSTAT 30/302 electrochemical workstation (Eco Chemie B.V., Amsterdam, The Netherlands) by employing a conventional three-electrode system with a graphite sheet (1 cm × 1 cm) and a Hg/HgO electrode as the counter and reference electrodes, respectively. The electrochemical properties of the as-synthesized $NiCo_2O_4$ modified electrode were evaluated by cyclic voltammetry (CV), galvanostatic charge−discharge (CD), and electrochemical impedance spectroscopy (EIS) in 6.0 M KOH solution at ambient conditions. EIS measurements were recorded at open circuit potential with a frequency loop from 100 kHz to 0.01 Hz, with an ac perturbation of 10 mV. The galvanostatic CD was used to examine the performance of the hybrid supercapacitor. The specific capacitance was calculated from the galvanostatic CD curves based on the following equation:[3,8,36]

$$C = \frac{I\Delta t}{\Delta V} \quad (1)$$

where C, I, Δt, and ΔV are the SC (F g^{-1}) of the electrodes, the discharging current density (A g^{-1}), the discharging time (s), and the discharging potential range (V), respectively.

3. RESULTS AND DISCUSSION

3.1. Physicochemical Characterization. TG and DTA measurements were initially performed to assess the follow-up calcination process of the as-prepared precursors. As depicted in Figure 1a, the sample undergoes a weight loss of 23.3% in

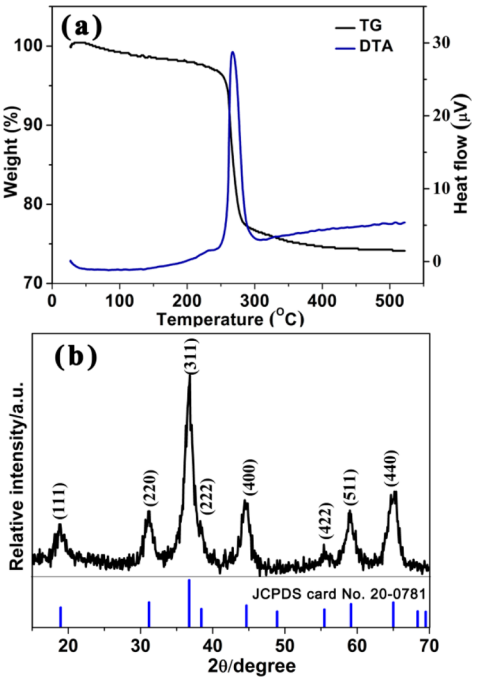

Figure 1. (a) TG (black) and DTA (blue) curves of the as-prepared precursors. (b) XRD pattern of the as-synthesized flower-shaped $NiCo_2O_4$.

the multistep weight loss process involving the dehydration and decomposition of precursors. The weight loss (1.5%) below 150 °C is ascribed to the removal of adsorbed water and the evaporation of the intercalated water molecules.[37] The subsequent weight loss (21.8%) with a strong exothermic peak at 250−300 °C arises from the loss of water and CO_2 generated by the dehydroxylation and decomposition of precursors.[38] At 300 °C, almost all the intercalated water molecules and gas molecules have escaped from the interslab space completely, leading to the formation of porous spinel $NiCo_2O_4$. At higher temperature, no obvious weight loss is observed indicating that there is no additional phase or structural change in $NiCo_2O_4$. Therefore, in order to obtain the $NiCo_2O_4$ with high purity, 300 °C is chosen as the calcination temperature.

The crystalline phase of the calcined black powder samples was identified by X-ray diffraction (XRD). As shown in Figure 1b, all of the diffraction peaks can be assigned to the spinel $NiCo_2O_4$ (JCPDS card No. 20-0781). Near absence of any secondary peaks in the XRD patterns clearly demonstrates the complete decomposition of the precursors to highly pure spinel $NiCo_2O_4$.

In order to further understand the elemental makeup and the oxidation state of as-prepared $NiCo_2O_4$, XPS measurements were implemented and the corresponding results were presented in Figure 2. The survey spectrum (Figure 2a) indicates the presence of Ni, Co, and O as well as C from the reference and the absence of other impurities. By using a Gaussian fitting method, the Ni 2p emission spectrum (Figure 2b) is best fitted considering two spin−orbit doublets characteristic of $Ni^{2+}$and Ni^{3+} and two shakeup satellites.[39] The fitting peaks at 855.7 and 873.1 eV are indexed to Ni^{2+}, while the other fitting peaks at 854.2 and 871.7 eV are ascribed to Ni^{3+}.[40] In Co 2p spectra (Figure 2c), two kinds of Co species can also be observed and assigned to the species containing Co(II) and Co(III) ions.[39,41] Specifically, the fitting peaks at binding energies (EB) of Co(II) ions at 780.7 and 795.8 eV are attributed to Co^{2+}, while the other two fitting peaks at 779.4 and 794.3 eV belong to Co^{3+}. The high-resolution spectrum for O 1s (Figure 2d) suggests three oxygen species marked as O1, O2, and O3. The fitting peak of O1 at 529.7 eV is typical of the metal−oxygen bond.[41,42] With respect to the component O2, the fitting peak sitting at 531.2 eV is commonly associated with defects, contaminants, and a number of surface species including hydroxyls, chemisorbed oxygen, under-coordinated lattice oxygen, or species intrinsic to the surface of the spinel.[39,41,43] The peaks at ∼532.6 eV could be attributed to multiplicity of physi- and chemisorbed water at or near the surface.[41,42] The O 1s spectra at binding energies of 529.7 and 531.2 eV are ascribed to O^{2-} species in $NiCo_2O_4$. These XPS results demonstrate that the electron couples of $Ni^{3+}/Ni^{2+}$and Co^{3+}/Co^{2+} are coexisting in the as-prepared flower-shaped $NiCo_2O_4$ sample. Thus, the formula of $NiCo_2O_4$ could be generally expressed as follows: $Co^{2+}{}_{1-x}Co^{3+}{}_{x}[Co^{3+}Ni^{2+}{}_{x}Ni^{3+}{}_{1-x}]O_4$ ($0 \le x \le 1$) (the cations within brackets are in octahedral sites and the outside ones are in tetrahedral sites), which is consistent with the results in the previous reports for $NiCo_2O_4$.[3,21]

The morphological and structural features of the as-synthesized flower-shaped microsphere samples were examined by SEM, TEM, HRTEM, and selected-area electron diffraction (SAED). Figure 3a displays the typical SEM image of the as-obtained precursors composed of many flower-shaped structures with diameter of about 1.5 μm. The inset in Figure 3a clearly displays the detailed morphology of an individual flower-shaped microsphere consisting of petal-like nanosheets. It can be distinctly observed that the nanopetals with a mean thickness of ∼15 nm and an average width of ∼1.0 μm attached to each other and constituted flower-shaped microsphere superstructure. After calcination of the precursors at 300 °C for 2 h, the obtained $NiCo_2O_4$ metal oxide materials (Figure 3b) still preserve the flower-shaped microsphere morphology,

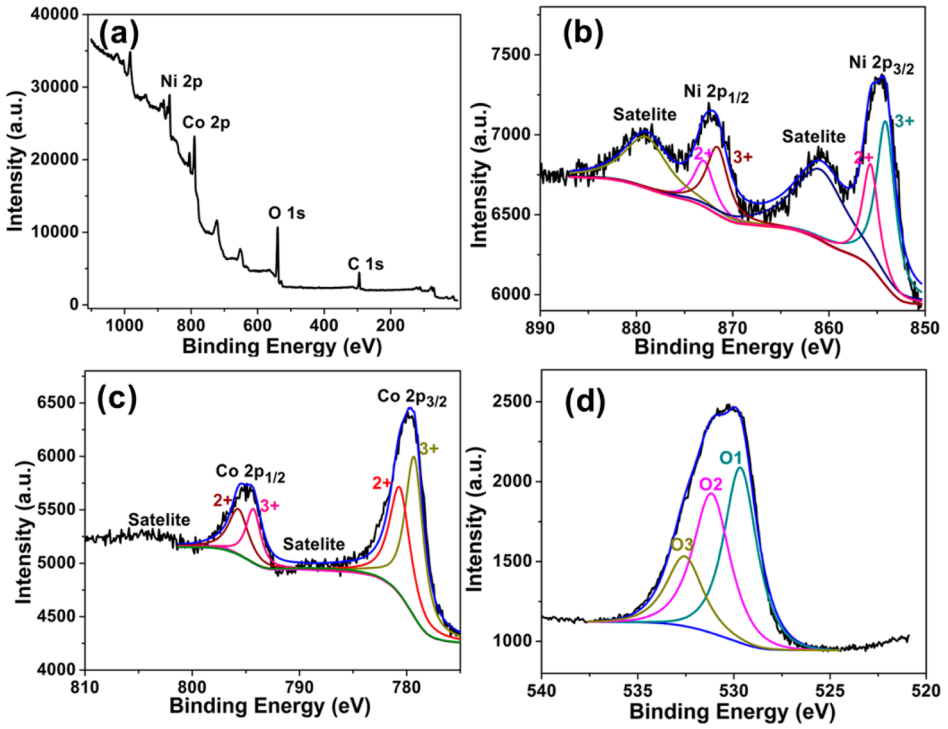

Figure 2. XPS spectra of (a) survey spectrum, (b) Ni 2p, (c) Co 2p, and (d) O 1s for flower-shaped mesoporous $NiCo_2O_4$ microspheres.

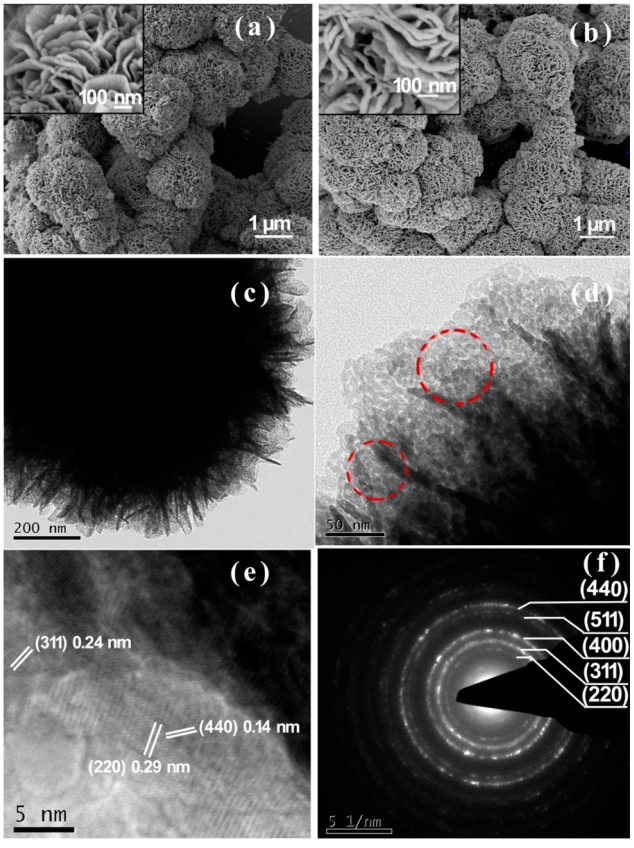

Figure 3. SEM images of (a) the as-obtained precursors and (b) the corresponding metal oxides after calcination. (c, d) TEM images, (e) HRTEM image, and (f) SAED pattern of the as-prepared $NiCo_2O_4$.

although the internal nanostructures may have been changed by opening pore channels due to the expulsion of CO_2 and H_2O gas during thermal decomposition process. Compared with the nanopetal-like structure (inset in Figure 3a) of precursors, the individual nanopetal structure (inset in Figure 3b) in calcined products also remains intact. Nevertheless, the average diameter of the corresponding $NiCo_2O_4$ metal oxides decreases, which is possibly caused by the collapse of part of the internal 3D porous structures during the thermal decomposition process.

The detailed morphological and crystallographic properties of the as-fabricated $NiCo_2O_4$ were identified by TEM, HRTEM, and SAED. Typical TEM image in Figure 3c obviously depicts a whole flower-shaped $NiCo_2O_4$ microsphere composed of petal-like nanostructures. Notably, the result illustrates that the as-prepared $NiCo_2O_4$ still maintained the intact flower-shaped microsphere morphology, which is consistent with the results from the SEM images. The magnified TEM image (Figure 3d) shows that nanopetals with a transparent feature on their edges are decorated with porous structures on their surface, which infers that it could provide high SSA.

The HRTEM image (Figure 3e) of an individual nanopetal with randomly orientated lattice phase reveals the polycrystalline characteristic of the as-harvested product. In addition, in the HRTEM image, the clearly resolved lattice fringes can be discerned and the lattice spacing is calculated to be about 0.29, 0.24, and 0.14 nm corresponding to the (220), (311), and (440) planes of spinel $NiCo_2O_4$, respectively. This result is in accord with that from the previous reports.[21,37] The SAED pattern (Figure 4f) displays well-defined rings, which further confirms that the samples are of polycrystalline nature, which is identical with the aforementioned results from XRD and HRTEM. It can be reckoned that such flower-shaped $NiCo_2O_4$ microspheres with fine porous structures and polycrystalline nature may be endowed with exciting electrochemical performance.

dx.doi.org/10.1021/am404765y | ACS Appl. Mater. Interfaces 2014, 6, 1773−1780

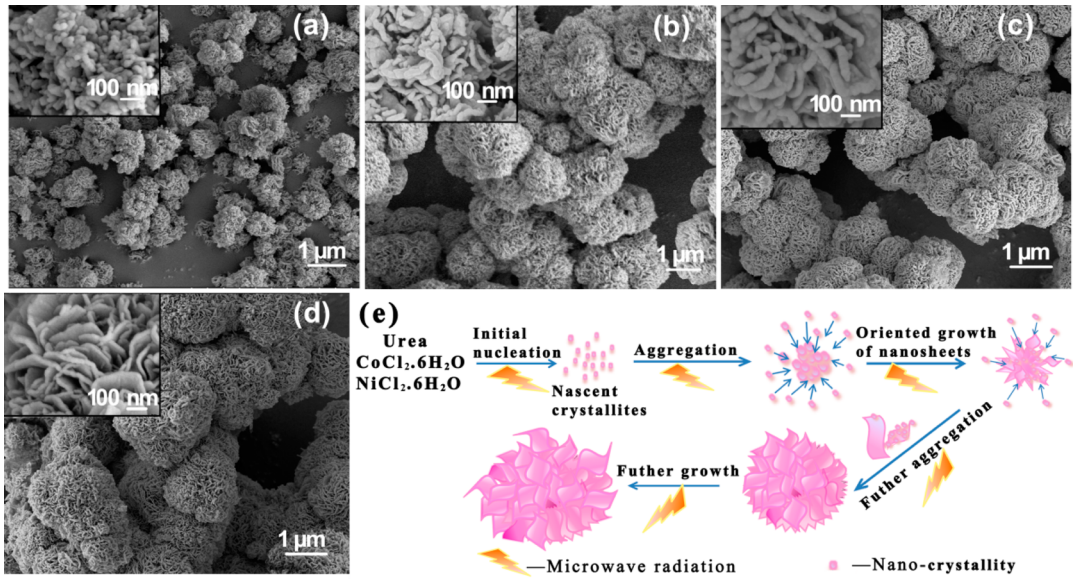

Figure 4. SEM images of the samples collected at different reaction times after the reaction temperature reached 100 °C: (a) 2 min, (b) 5 min, (c) 10 min, and (d) 15 min. (e) Schematic illustration of the morphological evolution of flower-shaped microsphere precursors.

To explore the formation mechanism of the flower-shaped microspheres, time-dependent experiments were carried out. FESEM and XRD were used to survey the morphologies and crystalline structures of as-collected precursors under different MAH durations after the reaction temperature reached 100 °C, respectively. As depicted in Figure 4a, within a very short time (ca. 2 min), the products composed of numerous nanoparticles aggregating together can be harvested. After microwave treatment for 5 min (Figure 4b), the samples exhibit prototypes of flower-shaped microstructures, which are composed of baby-size petal-like nanosheets. We also notice that some tiny nanoparticles attached to the surfaces of these small nanopetals, which might serve as the new growing points for other nanopetals in next stage. When the reaction time extends to 10 min (Figure 4c), the flower-like microstrustures are still underdeveloped with some small nanoparticles attached on some nanopetals. The full-grown flower-shaped microstructures constituted by more well-rounded nanopetals could be formed in the end (Figure 4d). All these show that the morphology and size of the products are significantly changed as reaction time goes by. The XRD patterns of the precursor collected at each reaction stage and its corresponding thermal decomposition product are displayed in Figure S1, Supporting Information. There is no change in the diffraction peak positions except the intensity of some diffraction peaks. The sample obtained at the initial reaction stage (ca. 2 min) is poorly crystallized (Figure S1a, Supporting Information). With an extension of reaction time, the intensity of diffraction peaks located around 12° and 59° is significantly enhanced, while those located around 22° and 35.5° gradually weaken until they disappear. These results illustrate that the growth of crystal undergoes a preferred orientation growth process.[44] The XRD patterns (Figure S1b, Supporting Information) of the corresponding thermal decomposition products also exhibit a similar change with the prolonged reaction time, which further confirms the preferred orientation crystal growth process.

On the basis of the above experimental observations, we have proposed a plausible mechanism (Figure 4e) for the morphological evolution process. The formation process of specific structures may involve a number of contributing factors such as hydrogen bonding, Vander Waals forces, electrostatic and dipolar fields, crystal-face attraction, and intrinsic crystal contraction.[29,44] It is reported that shape-controlled crystal growth can be achieved by manipulating the growth kinetics.[45,46] Since no organic additive, surfactant, or any template exist in the reaction, the concentrations of Co^{2+}, Ni^{2+}, and OH^- could play key roles.[44] Therefore, it may be more convincing to explain the process by employing the oriented attachment crystal growth model.[47] In the present case, accompanying the CO_3^{2-} and OH^- anions from hydrolysis of urea reacting with Co^{2+} and Ni^{2+} cations, a mountain of initial crystal nucleus start to come into being in the initial reaction stage. As the freshly formed nanonuclei are thermodynamically unstable due to their high surface energy, they tend to gather together to minimize the interfacial energy, and thus, the supersaturated nuclei could aggregate together. As the reaction proceeds, the reactants' concentration becomes lower, and some active sites on the surface of the initially formed precursor aggregations could grow along the oriented direction following the reaction environment constantly supplementing reactants. With new particles continuously depositing on the small raised areas of the agglomerates along specific oriented directions, some small petal-like structures form and further grow along the specific directions and thus constitute complete well-structured flower-shaped superstructures.

The specific surface area (SSA), average pore size, and mesoporous volume of materials play significant roles in enhancing electrochemical performance. With insight into the porosity of the as-prepared $NiCo_2O_4$, Brunauer–Emmett–Teller (BET) N_2-sorption measurements were implemented and the corresponding N_2 adsorption–desorption isotherm and pore size distribution were shown in Figure 5. As can be seen from Figure 5, a typical Langmuir type IV adsorption isotherm with a distinct type H3 hysteresis loop can be observed in the range of ca.0.5–1.0 P/P_0, which illustrates the existence of a mesoporous structure in sample. According to the investigative results, it is clear that the as-prepared 3D flower-shaped $NiCo_2O_4$ possesses a relatively high BET SSA of 148.5m^2 g^{-1}, which is larger than the previous reports.[21,37,48] The corresponding pore size distribution (inset of Figure 5)

dx.doi.org/10.1021/am404765y | ACS Appl. Mater. Interfaces 2014, 6, 1773–1780

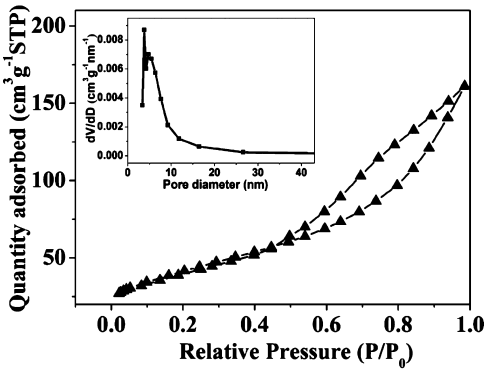

Figure 5. Nitrogen adsorption−desorption isotherm and the corresponding pore size distribution (inset) of flower-shaped $NiCo_2O_4$ mesoporous microspheres.

calculated by the Barrett−Joyner−Halenda (BJH) method from the desorption branch further confirms the characteristic of mesoporous structure.[49] A relatively narrow pore size distribution mainly centers in the range of 5−10 nm that is the optimal pore size for the diffusion of ions and electrons within the electrode.[37] With the characteristics of large SSA and porous structure, the 3D flower-shaped $NiCo_2O_4$ microspheres are considered to have potential application in supercapacitors, since the rich internal mesoporous structure could increase the electrode/electrolyte contact area and provide sufficient active sites for Faraday reaction and numerous channels for efficient transport of electrons and ions.

3.2. Electrochemical Characterization. To evaluate the potential of the as-synthesized $NiCo_2O_4$ acting as an electrode material for high rate supercapacitor, the electrochemical capacitive behavior was first elucidated by the CV method. Figure 6a depicts representative CV curves measured at various scan rates ranging from 2 to 30 mV s^{-1} in a potential range of 0.0−0.6 V (vs Hg/HgO) in 6.0 M KOH solution. The well-defined redox peaks are observed in anodic and cathodic sweeps in all CV curves, illustrating that the electrochemical capacitance of the $NiCo_2O_4$ superstructure electrode is mainly based on the redox mechanism. The redox peaks are mainly attributed to the redox reactions related to M−O/M−O−OH (M represents Ni or Co).[4] Interestingly, although two kinds of active centers for redox reaction from the solid state redox couples of Co^{2+}/Co^{3+} and Ni^{2+}/Ni^{3+} are present in the structures, there is no two couples of redox peaks of Ni^{2+}/Ni^{3+} and Co^{2+}/Co^{3+}, due to the similar redox potential of Co_3O_4 and NiO and the surface modification of $NiCo_2O_4$ by conductive acetylene black which can induce appreciable broadening of some redox peaks.[50] All CV curves (Figure 6a) exhibit a similar shape and the peak current increase with increasing scan rates. The shape of CVs changes little even at the high scan rate of 30 mV s^{-1}, indicating the good kinetic reversibility of the $NiCo_2O_4$ modified electrodes. Notably, the peak potential shifts only ca. 100 mV for a 15-time increase in the scan rate due to low polarization of the modified electrode. The inset in Figure 6a shows a good linear relationship of anodic and cathodic peak currents (i.e., current densities) vs the square root of the scan rate, demonstrating that the diffusion of OH^- is the rate controlling process in the whole process.

To quantify the SCs and the rate capability of the $NiCo_2O_4$-modified electrodes, galvanostatic CD measurements were carried out. Obviously, the nonlinearity in the discharge curves (Figure 6b) further verifies the pseudocapacitance behavior of $NiCo_2O_4$ coming from Faraday reaction. As shown in Figure 6c, with the increase of current density, the corresponding specific capacitance tends to decrease. Astonishingly, with an

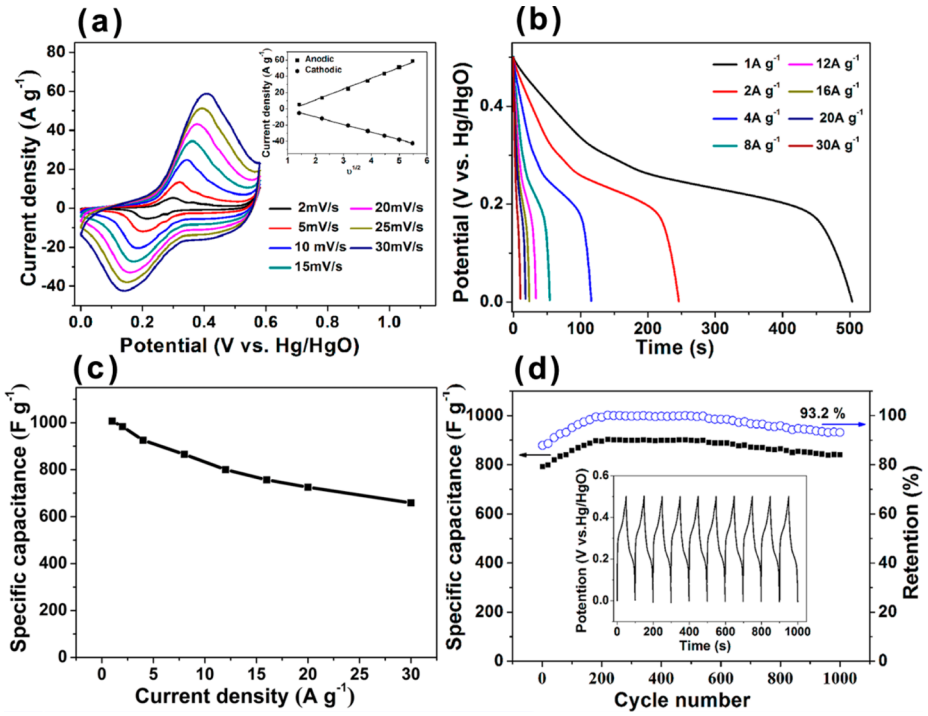

Figure 6. Electrochemical properties of the flower-shaped $NiCo_2O_4$ mesoporous microsphere: (a) CV curves at different scan rates (Inset: the plots of anodic and cathodic peak current density against the square root of the scan rate), (b) galvanostatic discharge curves at different current densities, (c) the corresponding specific capacitance as a function of current density, and (d) cycle performance at a current density of 8 A g^{-1}.

increase in the current density from 2 to 20 A g^{-1}, the specific capacitance value of the flower-shaped $NiCo_2O_4$ microspheres materials shows only a ~26% SC loss revealing its enhanced rate capability. Compared to the other reported similar spinel $NiCo_2O_4$ electrode materials[4,19,21,38,51−57] with different morphologies, the capacitance value obtained in our work is moderate, but the capacitance retention is remarkable (see Table S1, Supporting Information). As the current density increases, the capacitance value at 20 A g^{-1} remains to be 72.2% of that obtained at the current density of 1 A g^{-1}. Essentially, the considerable enhancement of capacitive performance at the quite high current density is attributed to better utilization of electroactive surface of the advantageous flower-shaped microsphere superstructure. The flower-shaped superstructure consisting of mesoporous nanopetals could provide numerous electroactive sites for Faraday reaction. In this case, the whole flower-shaped microsphere acting as an "ion-buffering reservoir" facilitates a quicker permeation process of electrolyte into each nanopetal-shaped matrix by shortening the diffusion distances of OH^- to the electroactive sites and accommodates the resulting strain caused by high rate insertion and extraction of OH^- ions. Therefore, even under the high current density, a large proportion of electroactive sites still remain, which conduces to enhancing the rate capability.

As shown in Figure 6d, cycle stability of the flower-shaped $NiCo_2O_4$-modified electrode at the current density of 8 A g^{-1} has been demonstrated. Interestingly, instead of decreasing, as in most cycle stability tests, the SC increases gradually over the initial 200 cycles accompanying the activation of active materials. Obviously, about 93.2% of the maximum SC can still be retained after 1000 continuous CD cycles, which reveals the flower-shaped $NiCo_2O_4$ microspheres possess the excellent long-term electrochemical stability even under the high current density.

The electrochemical performance of supercapacitor is partially affected by the charge-transfer resistance of electrode. EIS measurement was carried out to investigate the charge-transfer resistance. Figure 7 depicts the EIS of $NiCo_2O_4$-

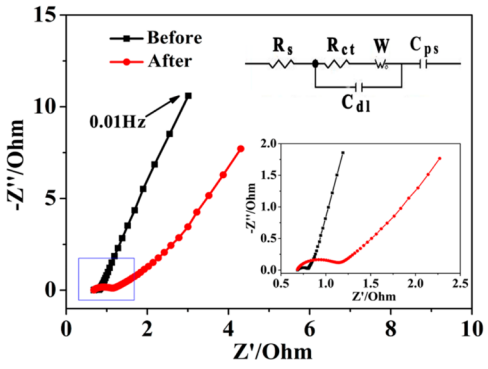

Figure 7. EIS plots of the as-synthesized $NiCo_2O_4$-modified electrode in 6.0 M KOH solution before and after the cycle test (Inset: the enlarged view of the high frequency region and the equivalent circuit diagram of different elements from the EIS analysis).

modified electrode measured before and after the CD cycle stability test. An equivalent circuit (inset of Figure 4) for fitting the EIS plots is composed of a bulk solution resistance R_s, a charge-transfer resistance R_{ct}, a double layer and a pseudocapacitive element C_{dl} and C_{ps}, and Warburg impedance W. The R_s and R_{ct} can be estimated from the intercepts of the high frequency semicircle with the real axis at R_s and (R_s + R_{ct}), respectively. The linear parts in the impedance plots at lower frequencies correspond to the W which is described as a diffusive resistance of the OH^- ion within the $NiCo_2O_4$ electrode pores. Both of the impedance spectra, composed of one high frequency semicircle related to R_{ct} followed by one linear component at the low frequency, are almost similar. The semicircle for the electrode before cycle test is quite small, and then the diameter is slightly larger after 1000 CD cycles, which indicates that the R_{ct} does not change much after the 1000-cycle test. This may benefit from the high conductivity of the flower-shaped $NiCo_2O_4$ microsphere and its robust 3D porous structure conducive to the fast ions/electrons transfer within the electrode and at electrode/electrolyte interface. After undergoing the 1000-cycle test, a slightly increased Warburg impedance can be observed due to the formation of inactive sites caused by the collapse of a part of the internal 3D porous structures during the cycle test. The results are good agreement with that from the long-term cycle stability test that SC degraded by less than 7% after 1000 cycles. Remarkably, even under the high current density, the $NiCo_2O_4$ electrode can still exhibit excellent electrochemical stability, which could be readily attributed to the interconnecting porous well-petaloid structures in the flower-shaped $NiCo_2O_4$ microspheres and their accommodation for the increased strain arising from fast insertion and extraction of OH^- ions during Faraday reaction.

4. CONCLUSION

In conclusion, we have successfully synthesized 3D flower-shaped $NiCo_2O_4$ microspheres via a sample and rapid MAH route followed by calcining at 300 °C. The 3D flower-shaped $NiCo_2O_4$ microsphere superstructure, composed of well-petaloid nanostructures, exhibited high SSA and porosity. The shape evolution of the 3D flower-shaped microspheres was investigated and a possible growth mechanism has been proposed. The further electrochemical investigations demonstrated that the flower-shaped $NiCo_2O_4$ microsphere as an electrode material for electrochemical capacitors displayed high specific capacitance (1006 F g^{-1} at 1 A g^{-1}), improved rate capability, and excellent cycle stability (93.2% retention after 1000 cycles) even at a high current density of 8 A g^{-1}. The enhanced electrochemical performance of the 3D flower-shaped $NiCo_2O_4$ mesoporous microsphere renders it an up-and-coming electrode material for high-performance supercapacitor.

■ ASSOCIATED CONTENT

Ⓢ Supporting Information

XRD patterns of the precursor and the corresponding $NiCo_2O_4$ products and a table comparing specific capacitance and capacitance retention of flower-shaped $NiCo_2O_4$ prepared in this work and of other nanostructured spinel materials reported in previous works. This material is available free of charge via the Internet at http://pubs.acs.org.

■ AUTHOR INFORMATION

Corresponding Author

*Tel: +86-28-85416029. Fax: +86-28-85415029. E-mail: xiaodan@scu.edu.cn.

Notes

The authors declare no competing financial interest.

■ ACKNOWLEDGMENTS

This work was financially supported by the Natural Science Foundation of China (Nos. 21177090, 21275104, and 21175094).

■ REFERENCES

(1) Simon, P.; Gogotsi, Y. *Nat. Mater.* **2008**, *7*, 845−854.
(2) Zhang, Y.; Feng, H.; Wu, X.; Wang, L.; Zhang, A.; Xia, T.; Dong, H.; Li, X.; Zhang, L. *Int. J. Hydrogen Energy* **2009**, *34*, 4889−4899.
(3) Yuan, C.; Li, J.; Hou, L.; Zhang, X.; Shen, L.; Lou, X. W. D. *Adv. Funct. Mater.* **2012**, *22*, 4592−4597.
(4) Wang, H.; Gao, Q.; Jiang, L. *Small* **2011**, *7*, 2454−2459.
(5) Vijayakumar, S.; Nagamuthu, S.; Muralidharan, G. *ACS Appl. Mater. Interfaces* **2013**, *5*, 2188−2196.
(6) Hu, C. C.; Chang, K. H.; Lin, M. C.; Wu, Y. T. *Nano Lett.* **2006**, *6*, 2690−2695.
(7) Hu, C. C.; Chen, W. C.; Chang, K. H. *J. Electrochem. Soc.* **2004**, *151*, A281−A290.
(8) Tian, X. Q.; Cheng, C. M.; Qian, L.; Zheng, B. Z.; Yuan, H. Y.; Xie, S. P.; Xiao, D.; Choi, M. M. *J. Mater. Chem.* **2012**, *22*, 8029−8035.
(9) Zhang, G.; Yu, L.; Hoster, H. E.; Lou, X. W. D. *Nanoscale* **2013**, *5*, 877−881.
(10) Wu, M. S.; Huang, K. C. *Chem. Commun.* **2011**, *47*, 12122−12124.
(11) Jiang, H.; Zhao, T.; Li, C.; Ma, J. *J. Mater. Chem.* **2011**, *21*, 3818−3823.
(12) Xia, X. H.; Tu, J. P.; Zhang, Y. Q.; Mai, Y. J.; Wang, X. L.; Gu, C. D.; Zhao, X. B. *RSC Adv.* **2012**, *2*, 1835−1841.
(13) Liu, X.; Long, Q.; Jiang, C.; Zhan, B.; Li, C.; Liu, S.; Zhao, Q.; Huang, W.; Dong, X. *Nanoscale* **2013**, *5*, 6525−6529.
(14) Li, M.; Xu, S.; Liu, T.; Wang, F.; Yang, P.; Wang, L.; Chu, P. K. *J. Mater. Chem. A* **2013**, *1*, 532−540.
(15) Mondal, C.; Ganguly, M.; Manna, P. K.; Yusuf, S.; Pal, T. *Langmuir* **2013**, *29*, 9179−9187.
(16) Mao, L.; Zhang, K.; Chan, H. S. O.; Wu, J. *J. Mater. Chem.* **2012**, *22*, 1845−1851.
(17) Lei, Z.; Zhang, J.; Zhao, X. *J. Mater. Chem.* **2012**, *22*, 153−160.
(18) Guo, Y. G.; Hu, J. S.; Wan, L. J. *Adv. Mater.* **2008**, *20*, 2878−2887.
(19) Wang, Q.; Liu, B.; Wang, X.; Ran, S.; Wang, L.; Chen, D.; Shen, G. *J. Mater. Chem.* **2012**, *22*, 21647−21653.
(20) Wei, T. Y.; Chen, C. H.; Chien, H. C.; Lu, S. Y.; Hu, C. C. *Adv. Mater.* **2010**, *22*, 347−351.
(21) Zou, R.; Xu, K.; Wang, T.; He, G.; Liu, Q.; Liu, X.; Zhang, Z.; Hu, J. *J. Mater. Chem. A* **2013**, *1*, 8560−8566.
(22) Jiang, H.; Ma, J.; Li, C. *Chem. Commun.* **2012**, *48*, 4465−4467.
(23) Hu, J. S.; Zhong, L. S.; Song, W. G.; Wan, L. J. *Adv. Mater.* **2008**, *20*, 2977−2982.
(24) Gnayem, H.; Sasson, Y. *ACS Catal.* **2013**, *3*, 86−861.
(25) Liu, W. M.; Gao, T. T.; Yang, Y.; Sun, Q.; Fu, Z. W. *Phys. Chem. Chem. Phys.* **2013**, *15*, 15806−15810.
(26) Wang, X.; Wu, X. L.; Guo, Y. G.; Zhong, Y.; Cao, X.; Ma, Y.; Yao, J. *Adv. Funct. Mater.* **2010**, *20*, 1680−1686.
(27) Ge, D.; Yang, L.; Tong, Z.; Ding, Y.; Xin, W.; Zhao, J.; Li, Y. *Electrochim. Acta* **2013**, *104*, 191−197.
(28) Ren, Y.; Gao, L. *J. Am. Ceram. Soc.* **2010**, *93*, 3560−3564.
(29) Meher, S. K.; Rao, G. R. *J. Phys. Chem. C* **2011**, *115*, 25543−25556.
(30) Meher, S. K.; Rao, G. R. *J. Power Sources* **2012**, *215*, 317−328.
(31) Chen, W.; Yan, L.; Bangal, P. R. *Carbon* **2010**, *48*, 1146−1152.
(32) Xu, L.; Ding, Y. S.; Chen, C. H.; Zhao, L.; Rimkus, C.; Joesten, R.; Suib, S. L. *Chem. Mater.* **2007**, *20*, 308−316.
(33) Cao, C. Y.; Guo, W.; Cui, Z. M.; Song, W. G.; Cai, W. *J. Mater. Chem.* **2011**, *21*, 3204−3209.
(34) Ding, Y.; Xu, L.; Chen, C.; Shen, X.; Suib, S. L. *J. Phys. Chem. C* **2008**, *112*, 8177−8183.
(35) Ai, Z.; Deng, K.; Wan, Q.; Zhang, L.; Lee, S. *J. Phys. Chem. C* **2010**, *114*, 6237−6242.
(36) Liu, M. C.; Kong, L. B.; Lu, C.; Li, X. M.; Luo, Y. C.; Kang, L. *ACS Appl. Mater. Interfaces* **2012**, *4*, 4631−4636.
(37) Qian, L.; Gu, L.; Yang, L.; Yuan, H. Y.; Xiao, D. *Nanoscale* **2013**, *5*, 7388−7396.
(38) Xiao, J.; Yang, S. *RSC Adv.* **2011**, *1*, 588−595.
(39) Roginskaya, Y. E.; Morozova, O.; Lubnin, E.; Ulitina, Y. E.; Lopukhova, G.; Trasatti, S. *Langmuir* **1997**, *13*, 4621−4627.
(40) Kim, J. G.; Pugmire, D.; Battaglia, D.; Langell, M. *Appl. Surf. Sci.* **2000**, *165*, 70−84.
(41) Marco, J.; Gancedo, J.; Gracia, M.; Gautier, J.; Rıos, E.; Berry, F. *J. Solid State Chem.* **2000**, *153*, 74−81.
(42) Choudhury, T.; Saied, S.; Sullivan, J.; Abbot, A. *J. Phys. D: Appl. Phys.* **1989**, *22*, 1185.
(43) Zhong, J. H.; Wang, A. L.; Li, G. R.; Wang, J. W.; Ou, Y. N.; Tong, Y. X. *J. Mater. Chem.* **2012**, *22*, 5656−5665.
(44) Li, B.; Wang, Y. *J. Phys. Chem. C* **2009**, *114*, 890−896.
(45) Li, B. X.; Jing, M.; Rong, G. X.; Xu, Y.; Xie, Y. *Eur. J. Inorg. Chem.* **2006**, *21*, 4349.
(46) Zhang, D. F.; Sun, L. D.; Zhang, J.; Yan, Z. G.; Yan, C. H. *Cryst. Growth Des.* **2008**, *8*, 360.
(47) Penn, R. L.; Banfield, J. F. *Science* **1998**, *281*, 969−971.
(48) Li, L. L.; Cheah, Y.; Ko, Y.; Teh, P.; Wee, G.; Wong, C. L.; Peng, S. J.; Srinivasan, M. *J. Mater. Chem. A* **2013**, *1*, 10935−10941.
(49) Li, J.; Xiong, S.; Liu, Y.; Ju, Z.; Qian, Y. *ACS Appl. Mater. Interfaces* **2013**, *5*, 981−988.
(50) Meher, S. K.; Rao, G. R. *J. Phys. Chem. C* **2011**, *115*, 15646−15654.
(51) Lu, Q.; Chen, Y.; Li, W.; Chen, J. G.; Xiao, J. Q.; Jiao, F. *J. Mater. Chem. A* **2013**, *1*, 2331−2336.
(52) Yuan, C.; Li, J.; Hou, L.; Yang, L.; Shen, L.; Zhang, X. *J. Mater. Chem.* **2012**, *22*, 16084−16090.
(53) Wu, T.; Li, J.; Hou, L.; Yuan, C.; Yang, L.; Zhang, X. *Electrochim. Acta* **2012**, *81*, 172−178.
(54) Yu, L.; Wu, H.; Wu, T.; Yuan, C. *RSC Adv.* **2013**, *3*, 23709−23714.
(55) Chang, J.; Sun, J.; Xu, C.; Xu, H.; Gao, L. *Nanoscale* **2012**, *4*, 6786−6791.
(56) Xu, K.; Zou, R.; Li, W.; Xue, Y.; Song, G.; Liu, Q.; Liu, X.; Hu, J. *J. Mater. Chem. A* **2013**, *1*, 9107−9113.
(57) Xiao, Y.; Liu, S.; Li, F.; Zhang, A.; Zhao, J.; Fang, S.; Jia, D. *Adv. Funct. Mater.* **2012**, *22*, 4052−4059.